Research Square

Preprints are preliminary reports that have not undergone peer review.
They should not be considered conclusive, used to inform clinical practice,
or referenced by the media as validated information.

Quantifying the long-term evolution of post-earthquake debris-flow activity in the epicentral area of the 2008 Wenchuan earthquake, China

Qingyun Shi

shiqingyun@cuit.edu.cn

Chengdu University of Information Technology

Chuan Tang

Chengdu University of Technology

Weihua Zhang

Climate Center of Tibet Autonomous Region

Yucai Ma

Climate Center of Tibet Autonomous Region

Wei Zhou

Chengdu University of Technology

Jiang Xiong

Chinese Academy of Sciences Chengdu Institute of Mountain Hazards and Environment

Yu Tie

Chengdu Zhongke Nengsin Technology

Research Article

Keywords: LSSP, Debris flow activity intensity, Quantitative prediction, Long-term evolution, Wenchuan earthquake

Posted Date: June 4th, 2026

DOI: https://doi.org/10.21203/rs.3.rs-9629002/v1

License: This work is licensed under a Creative Commons Attribution 4.0 International License.
Read Full License

Quantifying the long-term evolution of post-earthquake debris-flow activity in the epicentral area of the 2008 Wenchuan earthquake, China

Qingyun Shi[a,b], Chuan Tang[c*], Weihua Zhang[d], Yucai Ma[d], Wei Zhou[b], Jiang Xiong[e], Yu Tie[f]

[a] College of Resources and Environment, Chengdu University of Information Technology, Chengdu, 610225, China

[b] Key Laboratory of Meteorological Remote Sensing and Disaster Accident Prevention and Control, Sichuan Provincial Department of Education, Chengdu 610054, China

[c] State Key Laboratory of Geohazard Prevention and Geoenvironment Protection, Chengdu University of Technology, Chengdu 610054, China

[d] Climate Center of Tibet Autonomous Region, Lasha 850000, China

[e] Key Laboratory of Mountain Hazards and Earth Surface Processes, Institute of Mountain Hazards and Environment, Chinese Academy of Sciences, Chengdu 610299, China

[f] Chengdu Zhongke Nengsin Technology Co. Chengdu 610041, China

Abstract

The 2008 Wenchuan earthquake triggered widespread coseismic landslides and supplied large volumes of loose material on hillslopes and channels, resulting in persistent post-earthquake debris flow activity near the epicentral area. Quantifying the long-term evolution of this activity is important for geohazard assessment, but remains challenge because debris flows are jointly controlled by sediment supply, topography, and rainfall. In this study, a catchment-scale framework was developed to evaluate debris flow activity intensity in 44 catchments affected by the Wenchuan earthquake. Multi-temporal landslide inventories from 2008 to 2019 were used to calculate landslide sediment supply potential (LSSP), which integrates landslide areal density,

spatial distribution indices, and channel gradient. LSSP was then combined with representative hourly rainfall intensities from documented debris flow triggering events to derive a debris flow activity intensity index (AI_{DF}). The results show that active landslide area decreased from 122.05 km² in 2008 to 30.55 km² in 2019, while recovery areas expanded progressively. LSSP increased sharply immediately after the earthquake and then declined over time, with a rapid decrease during 2008–2011 followed by a slower adjustment phase. Nevertheless, sediment supply in many catchments remained above the pre-earthquake level in 2019. AI_{DF} showed an overall decline after its post-earthquake peak, although temporary increases occurred during major rainfall events. Comparison with documented debris flow events indicates that AI_{DF} captures the main temporal pattern of observed activity. The fitted long-term trend suggests three stages of post-earthquake debris flow activity: an active period from 2008 to 2013, a recession period from 2013 to 2048, and a relatively stable period after 2048. These results indicate that debris flow activity in the Wenchuan earthquake-affected area may persist for several decades, mainly controlled by the gradual depletion and redistribution of landslide-derived sediment under rainfall forcing.

Key words: LSSP; Debris flow activity intensity; Quantitative prediction; Long-term evolution; Wenchuan earthquake

1. Introduction

Earthquake-triggered landslides and their subsequent transformation into debris flows represent one of the most destructive cascading geohazard processes in

mountainous regions worldwide. Large earthquakes can instantaneously generate enormous volumes of loose, unconsolidated material, fundamentally alter hillslope-channel systems and create highly unstable geomorphic conditions (Fan et al., 2019a; Keefer, 1984; Parker et al., 2011). These materials are readily remobilized by rainfall, frequently producing debris flows that pose long-lasting threats to downstream communities, infrastructure, and ecosystems (Iverson, 1997; Takahashi, 1981; Tang et al., 2012a). Compared with coseismic landslides, post-earthquake debris flows often exhibit stronger temporal persistence and broader spatial impacts, making them a critical component of multi-hazard chains in tectonically active regions (Utley et al., 2025; Yang et al., 2023).

Globally, numerous catastrophic debris flow disasters have been documented following major earthquakes, highlighting their significance. For example, after the 1999 Chi-Chi earthquake in Taiwan and the 2015 Gorkha earthquake in Nepal, intense rainfall triggered widespread debris flows that caused severe casualties and infrastructure damage (Kargel and Hudnut, 2016; Lin et al., 2006). Similarly, the 2008 Wenchuan earthquake in China triggered widespread landsliding, generating abundant loose material that has played a critical role in subsequent debris flow activity (Xu et al., 2014). These materials have since been repeatedly remobilized during rainfall events, producing numerous catastrophic debris flows over more than a decade (Huang and Li, 2014; Tang et al., 2019; Yang et al., 2017b). Importantly, field investigations and remote sensing analyses indicate that more than 70% of coseismic debris may

remain stored in the landscape for extended periods, sustaining high debris flow susceptibility for decades (Fan et al., 2018; Zhang and Zhang, 2017).

The long-term evolution of debris flow activity in post-earthquake environments is governed by complex interactions among three primary factors: (i) the availability and spatial distribution of loose material, (ii) topographic conditions controlling sediment transport efficiency, and (iii) rainfall characteristics that trigger debris flow initiation (Iverson, 1997; Takahashi, 1981). In the years immediately following an earthquake, abundant loose material and low rainfall thresholds typically lead to high debris flow activity. Over time, processes such as material depletion, grain coarsening, and vegetation recovery progressively modify these conditions, resulting in dynamic changes in debris flow frequency and magnitude (Domènech et al., 2019; Huang, 2011). Understanding how these factors co-evolve and jointly control debris flow activity is therefore essential for long-term hazard assessment.

Previous studies have investigated post-earthquake geohazards from multiple perspectives, including the temporal evolution of landslides (Fan et al., 2018; Shi et al., 2021; Xiong et al., 2021), vegetation recovery processes (Shen et al., 2020; Yang et al., 2020; Yang et al., 2017a), and rainfall thresholds for debris flow initiation (Cui et al., 2010; Guo et al., 2017). Some studies have also examined the evolution of debris flow activity using empirical or statistical approaches (Yang et al., 2023; Zhang et al., 2023). Based on variations in the availability of loose material, previous studies have suggested that the elevated occurrence of geohazards in the Wenchuan earthquake

region may persist for approximately 20–25 years (Huang, 2011). Debris flow formation processes have been investigated by integrating factors such as loose material, micro-topography, and hydrological conditions (Cui et al., 2010). However, these studies are primarily event-based or qualitative in nature and do not provide a quantitative framework for evaluating the long-term evolution of debris flow activity at the catchment scale.

Despite these advances, significant knowledge gaps remain. First, most existing studies focus on individual controlling factors or limited combinations thereof, and few attempts have been made to quantitatively integrate sediment supply, topography, and rainfall within a unified framework (Cui et al., 2010; Guo et al., 2017; Li et al., 2018), particularly in a manner that explicitly links sediment supply dynamics to long-term debris-flow activity following large earthquakes. Second, current studies on post-earthquake debris flow evolution are largely descriptive or empirical, lacking quantitative models capable of predicting long-term variations in debris-flow activity intensity at the catchment scale (Fan et al., 2018; Zhang et al., 2023). Third, the role of landslide-derived sediment supply as a dynamic and spatially heterogeneous control on debris-flow activity has not been fully quantified, particularly in terms of its interaction with rainfall and topography (Fan et al., 2019b; Iverson, 1997).

To address these limitations, this study develops an integrated quantitative framework to evaluate the long-term evolution of debris-flow activity in the Wenchuan earthquake-affected area. By incorporating sediment supply, topography, and rainfall

forcing, the framework enables assessment of debris-flow activity at the catchment scale. The framework is then used to analyze the temporal evolution of landslide-derived sediment, examine its spatial controls on debris flow initiation, and estimate long-term variations in debris-flow activity intensity. This work provides a quantitative basis for linking sediment-supply dynamics with debris-flow activity and may support long-term hazard assessment in earthquake-affected mountain catchments.

2. Study area

The study area is located in the Wenchuan earthquake-affected region, Sichuan Province, China, and comprises 44 catchments covering approximately 440 km² near the earthquake epicenter (Fig. 1). Catchment areas range from 0.40 to 51.71 km², with relief ranging from 0.86 to 3.16 km (Table 1), while detailed information for individual catchments is provided in Table S1. The terrain is characterized by rugged mountains and deeply incised valleys, with elevations from 550 to 5600 m a.s.l., providing favorable conditions for rapid runoff concentration and sediment transport.

The 2008 Mw 7.9 Wenchuan earthquake triggered more than 200,000 landslides, generating abundant unconsolidated material that was subsequently stored on hillslopes and within channels (Xu et al., 2014). Bedrock in the region is highly fractured and strongly weathered, with well-developed fault systems (notably the Wenchuan–Maowen and Yingxiu–Beichuan faults) and pervasive joints and bedding planes, which further enhance slope instability and sediment availability (Fan et al., 2018; Tang et al., 2011).

The study area is drained mainly by the Minjiang and Yuzixi rivers. The Minjiang River originates in the northwestern mountainous region and forms part of the upper Yangtze River system, whereas the Yuzixi River drains the southwestern part of the study area near Wolong town (Fig. 1) (Fan et al., 2018). The study area has a subtropical monsoon climate, with mean annual precipitation of approximately 1250 mm and a mean annual temperature of about 13°C. Intense rainfall during the wet season is a key trigger of debris flows (Tang et al., 2011).

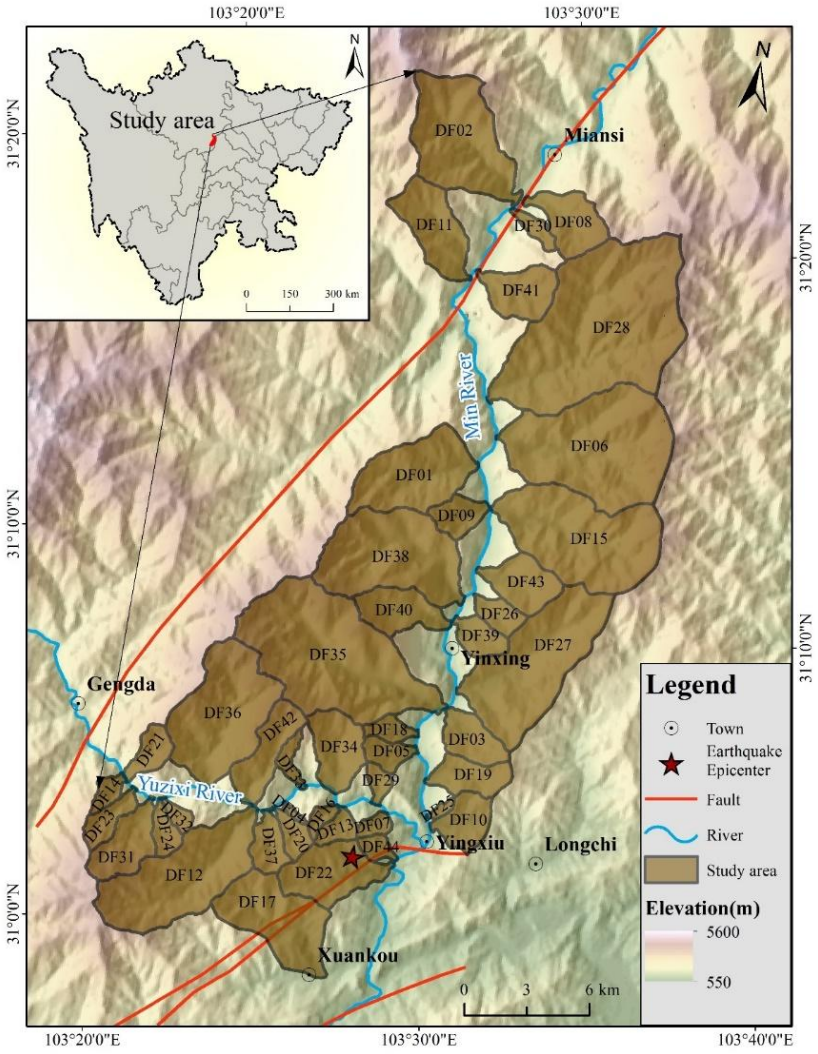


Fig. 1 Overview of the study area.

Table 1 Summary statistics of topographic metrics for debris flow catchments. Detailed values for

individual catchments are provided in Table S1.

Parameter	Min	Max	Mean
Area (km²)	0.4	51.71	10.10
Channel length (km)	1.17	14.18	4.83
Relief (km)	0.86	3.16	1.98
Channel gradient (‰)	209.52	759.33	496.53

3. Material and methods

To provide a clear overview of the methodological framework, Fig. 2 summarizes the workflow adopted in this study. The approach integrates multi-temporal landslide inventory mapping, sediment supply assessment, topographic analysis, and rainfall forcing to evaluate the long-term evolution of debris-flow activity in the Wenchuan earthquake-affected area. Sediment supply conditions are characterized using three complementary aspects: the amount of available loose material, its spatial distribution within the catchment, and the topographic potential for mobilization. These aspects are represented by landslide areal density, spatial distribution indices, and channel gradient, respectively. The derived sediment supply potential is then combined with rainfall forcing to assess debris-flow activity intensity and its temporal evolution.

The framework highlights the coupling among sediment supply, topography, and rainfall, and provides a quantitative basis for assessing long-term debris-flow activity at the catchment scale.

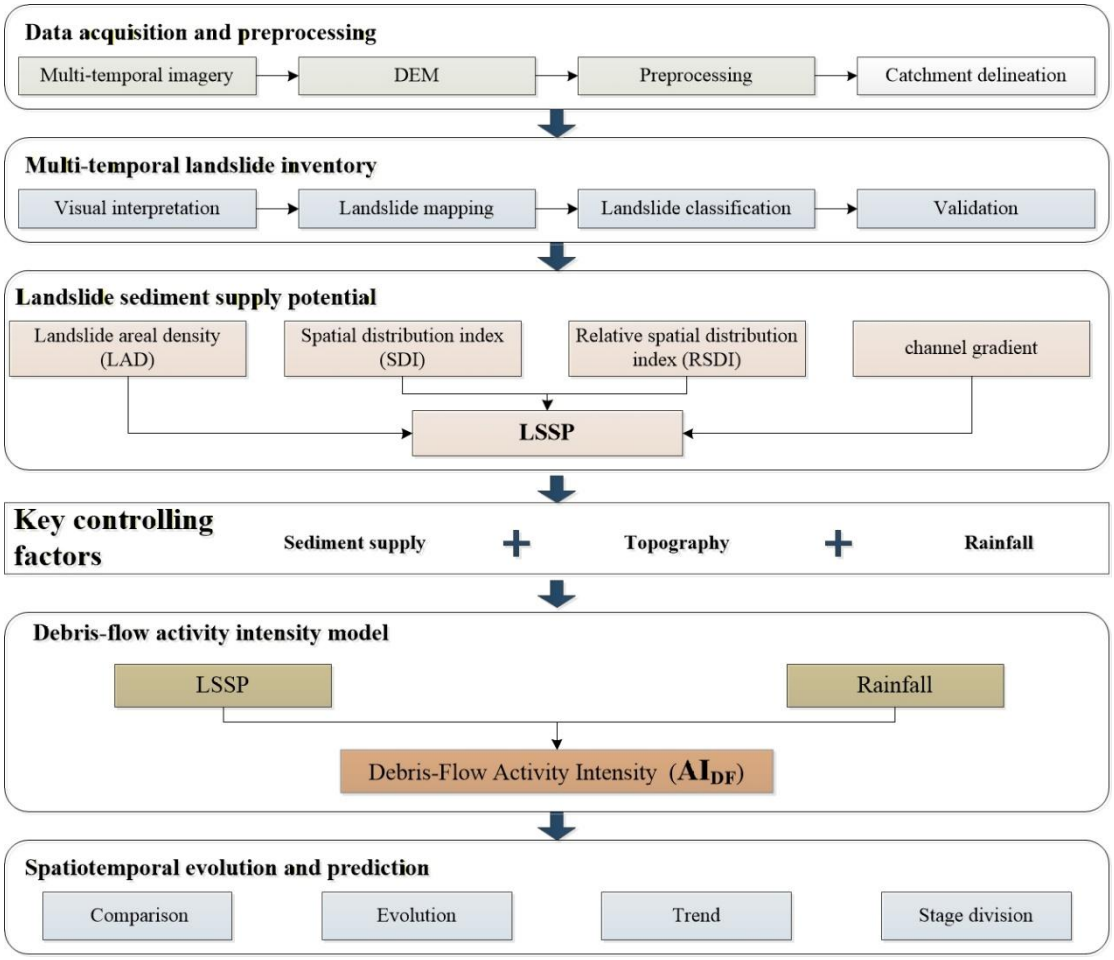


Fig. 2 Methodological framework for reconstructing landslide-derived sediment supply and modelling the long-term evolution of debris-flow activity in the Wenchuan earthquake-affected area.

3.1. Data acquisition and preprocessing

Multi-temporal remote sensing images and aerial photographs, including Spot-5, Worldview-2, ZY-1, GF-1, and Google Earth images, were collected to facilitate visual interpretation and identification of landslides. A total of six images taken in 2008, 2011, 2012, 2013, 2015 and 2019 were selected for landslide inventory mapping from 2008 to 2019, considering factors such as resolution, cloud cover and date of acquisition (Table 2). Additionally, the landslide inventories for 2005 and 2007, obtained from a previous study (Fan et al., 2019), were incorporated to track pre-earthquake changes in

166 landslide areas.

167 To ensure accurate and reliable mapping results, the acquired images underwent
168 geometric correction within the ENVI and ArcGIS platforms. A 10 m resolution Digital
169 Elevation Model (DEM) supplied by the State Key Laboratory of Geological Hazard
170 Prevention and Geoenvironmental Protection (SKLGP) was used in this process.
171 Ground control points (GCP) and the DEM were employed to correct the images to
172 mitigate the effects of topography, image distortion, and mismatches. The DEM also
173 facilitated delineation of catchment boundaries and extraction of essential terrain
174 characteristics, such as channels, elevation, and slope. Table 2 lists the detailed
175 information of these datasets.

176 **Table 2** Data used in this research. The source, acquisition date and attributes of each layer
177 contained in the dataset.

Type	Source	Acquisition date	Resolution (m)	Usage
Satellite image	UAV	2008.06	1	Images generating landslide inventories
	Spot-5	2008.07	2.5	
	Worldview-2	2011.04	1	
	Spot 5	2012.04	2.5	
	ZY-1 02C	2013.02	5	
	GF-1	2015.04	2	
	Google earth	2019.10	1	
DEM	SKLGP	2010	10	Extracting catchment

3.2. Multi-temporal landslide inventory

A pre-earthquake landslide inventory for the years 2005 and 2007, delineated by a previous study, was used as a reference for pre-earthquake landslide conditions within a short-term observation window. Although the available pre-event data are limited, previous studies have indicated that landslide activity in the study area was relatively low before the Wenchuan earthquake (Fan et al., 2019). Therefore, these inventories provide a baseline for comparing the large post-earthquake changes rather than a complete reconstruction of pre-earthquake debris-flow activity. After the Wenchuan earthquake, 2008 imagery was used to delineate coseismic landslides, while images from 2011, 2012, 2013, 2015 and 2019 were used to identify new landslides and assess the remobilization of coseismic deposits.

The landslide-affected areas were classified into five categories based on visual interpretation and comparison of multi-temporal remote sensing images: coseismic landslides (CL), enlarged landslides (EL), new landslides (NL), dormant landslides (DL), and recovery areas (RA) (Li et al., 2018; Shi et al., 2021). CL were mapped from the 2008 post-earthquake imagery, whereas NL and EL were identified from subsequent images as newly formed landslides and expansions of previously mapped landslides, respectively. DL refers to landslides that remained identifiable but showed no obvious renewed activity, while RA denotes previously mapped landslide areas that showed surface recovery, such as reduced exposed material or vegetation regrowth, with no

198 evident remobilization. In this study, “landslide” refers to slope failures involving the
199 downslope movement of rock, soil, or debris (Zhang and Zhang, 2017).

200 The inventories were derived from multi-temporal remote sensing images through
201 visual interpretation using consistent criteria. Where possible, higher-resolution
202 imagery was used to refine landslide boundaries, and multi-temporal images were
203 cross-checked to ensure consistency in identification and classification. Although
204 differences in image resolution may introduce some uncertainty, the analysis focuses
205 on catchment-scale patterns and temporal evolution, and the influence of local
206 delineation uncertainty is therefore considered limited.

207 3.3. Landslide sediment supply potential

208 To quantitatively represent sediment supply conditions relevant to debris flow
209 initiation, it is necessary to consider not only the amount of available material, but also
210 its spatial distribution and its mobilization potential. These aspects cannot be
211 adequately captured by a single metric. Therefore, this study adopts three
212 complementary indicators: landslide areal density to represent the magnitude of
213 sediment supply, spatial distribution indices to describe the positioning of loose
214 material within the catchment, and channel gradient to reflect the potential for material
215 mobilization.

216 3.3.1. Landslide areal density index

217 Landslide areal density (LAD) was used to represent the amount of landslide-
218 derived loose material available within each catchment. This indicator can be

consistently derived from multi-temporal remote sensing images and provides a catchment-scale measure of active sediment sources (Wu et al., 2012). For each catchment, A_{ca} was calculated from the DEM-derived catchment polygon, while A_{ac} was obtained by overlaying the landslide inventory with the catchment boundary and summing the areas of CL, NL, EL, and DL. RA was excluded because it represents recovered or inactive areas. LAD is calculated as follows:

$$LAD = {}^{A_{ac}}/_{A_{ca}} \quad (1)$$

where LAD is the landslide areal density, a dimensionless ratio; A_{ac} is the total area of CL, NL, EL, and DL within the catchment (km^2), and A_{ca} is the area of catchment (km^2).

3.3.2. Distribution index of landslides

While the amount of loose material is important, its spatial distribution within a catchment also controls whether it can be mobilized into debris flows. Material located close to the main channel or catchment outlet is more likely to be entrained during rainfall events, whereas material distributed on distal hillslopes or at higher elevations may remain less connected to the transport pathway (Fan et al., 2019b; Iverson, 1997; Tang et al., 2012a). Here, the catchment outlet refers to the downstream exit point of the catchment. For example, two catchments with similar landslide areas may exhibit different debris flow responses if loose material is concentrated near the main channel in one catchment but more widely dispersed in the other. Therefore, spatial distribution indices are introduced to quantify the relative position of landslide-derived material within the catchment.

(1) Spatial distribution index

To quantify the elevation-related distribution of landslide-derived loose material, the spatial distribution function T and spatial distribution index (SDI) were introduced following Fan et al. (2012). The function T describes the relationship between landslide area and relative elevation, whereas SDI summarizes this distribution into a single value. They are defined as follows:

$$s=S/A \tag{2}$$

$$T=h/H \tag{3}$$

$$T = T(s) \ \ (T\in[0,1],\ s\in[0,1]) \tag{4}$$

$$SDI=\int_0^1 T(s)ds \tag{5}$$

where T is the relative elevation ratio, calculated as the elevation difference between a given contour line and the lowest point of the catchment divided by the total catchment relief (dimensionless); s is the cumulative landslide-area ratio, calculated as the area of active landslides above the corresponding contour line divided by the total active landslide area in the catchment (dimensionless); h is the relative elevation difference between each contour and the lowest point in the catchment (m); H is the total catchment relief, i.e., the elevation difference between the highest and lowest points of the catchment (m); S is the area of active landslides above the corresponding contour line (m^2); A is the total area of active landslides in the catchment (m^2). The SDI is calculated by integrating T(s) with respect to s from 0 to 1, and is therefore dimensionless. Unlike LAD, SDI does not quantify the amount of landslide area, but

256 describes the elevation-related distribution of landslide-derived loose material within
257 the catchment.

258 The spatial distribution function reflects the relative distribution of loose material
259 with elevation. When loose material is uniformly distributed, the function follows
260 $T=1-s$. A gentler segment of the curve indicates concentration within the corresponding
261 elevation interval, whereas a steeper decline indicates sparse distribution (Fig. 3a). SDI
262 further indicates whether loose material is preferentially distributed at higher or lower
263 elevations. SDI = 0.5 indicates an even distribution across elevation intervals; SDI >
264 0.5 indicates a higher-elevation concentration; and SDI < 0.5 indicates a lower-
265 elevation concentration, where material is generally more connected to downstream
266 flow pathways and more likely to contribute to debris-flow activity (Fig. 3a).

267 (2) Relative spatial distribution index

268 In addition to elevation-related distribution, the distance of landslide-derived
269 material from the catchment outlet and main channel also affects its likelihood of
270 mobilization. Material located closer to these flow pathways is more readily delivered
271 to debris flows during rainfall events. Therefore, the relative spatial distribution
272 function F and relative spatial distribution index (RSDI) were introduced to quantify
273 the proximity of loose material to the catchment outlet and main channel (Fan et al.,
274 2012). They are defined as follows:

$$x = {}^{a}/_{A} \tag{6}$$

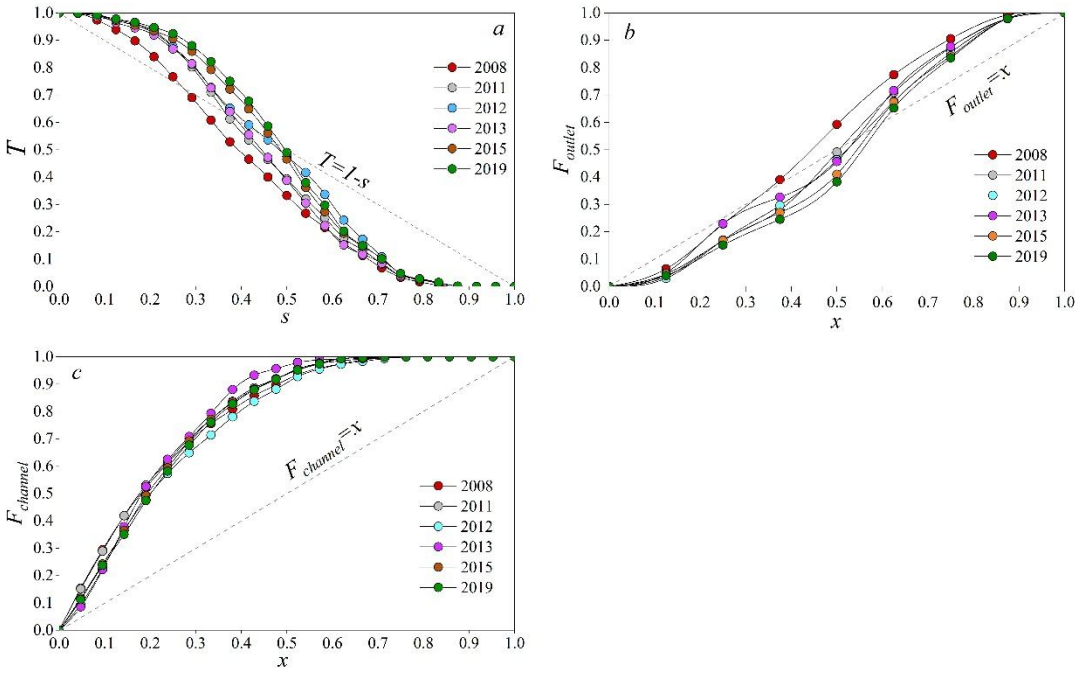
$$F = {}^{1}/_{L} \tag{7}$$

$$F=F(x) \quad (F \in [0,1], x \in [0,1]) \tag{8}$$

$$RSDI=\int_0^1 F(x)dx \tag{9}$$

where F is the relative distance function (dimensionless), x is the cumulative landslide-area ratio (dimensionless), l is the distance between the landslides and the outlet or main channel in the catchment (m); L is the maximum distance of the catchment boundary from the outlet or the main channel (m); a is the area of active landslides within the corresponding distance interval from the catchment outlet or main channel (m^2); A is the total area of active landslides in the catchment (m^2). RSDI is dimensionless.

The relative spatial distribution function describes the relationship between the distribution of loose material and its distance from the catchment outlet or main channel. When loose material is uniformly distributed relative to these reference features, the function follows $F(x)=x$. A gentler segment of the curve indicates concentration within the corresponding distance range, whereas a steeper variation indicates a more dispersed distribution (Fig. 3b and Fig. 3c).



287

288 **Fig. 3** Spatial distribution functions (a) and relative spatial distribution functions (b and c) for

289 landslides within Chediguan catchment. T=1-s, indicating that active landslides are uniformly

290 distributed throughout the elevation interval; $F_{outlet}=x$ or $F_{channel}=x$, indicating that active landslides

291 distributed evenly relative to the outlet or main channel of catchment.

292 Unlike SDI, which describes elevation-related distribution, RSDI measures the

293 proximity of loose material to the catchment outlet or main channel. A larger RSDI

294 indicates that loose material is located closer to the main sediment-transfer pathway

295 and is therefore more likely to be mobilized into debris flows. A smaller RSDI indicates

296 weaker spatial connectivity to the outlet or main channel.

297 Buffer analysis was performed in ArcGIS using the catchment outlet and main

298 channel as reference features. A buffer interval of 100 m was adopted to balance spatial

299 resolution and mapping uncertainty. Smaller intervals may amplify errors associated

300 with landslide delineation, whereas larger intervals may obscure meaningful spatial

patterns (Fig. 4). MATLAB was then used to fit the distribution functions, and SDI and RSDI were calculated according to Equations. (5) and (9).

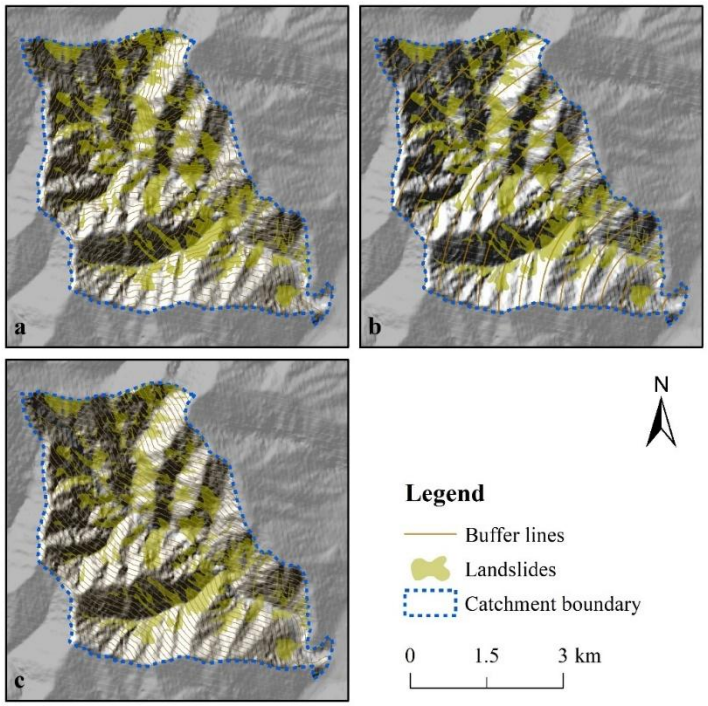


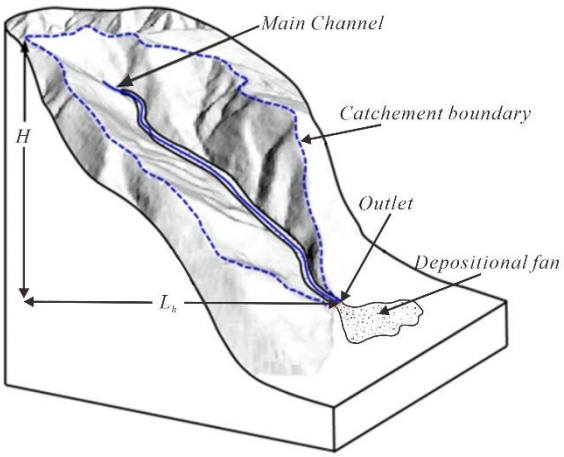
Fig. 4 Spatial distribution of landslides in specific catchment. (a) spatial distribution of landslides, (b) and (c) spatial distributions relative to the catchment outlet and main channel, respectively.

(3) Channel gradient index

Channel gradient (J) was used to represent the topographic potential for mobilizing loose material. Steeper channels favor the conversion of potential energy to kinetic energy and promote debris flow initiation (Zhou et al., 2019). J was calculated as the ratio of catchment relief, defined as the elevation difference between the maximum elevation and the fan apex, to the horizontal projection length of the main channel (L_h)(Fig. 5).

In the study area, catchment relief ranges from 0.86 to 3.16 km, main channel length from 1.17 to 14.18 km, and channel gradient from 209.52‰ to 759.33‰ (Table

315 S1). These steep topographic conditions favor rapid runoff concentration and provide
316 suitable conditions for debris flow initiation.



317

318 **Fig. 5** Parameters measured in the debris flow catchments. Cited and modified from (Zhou et al.,
319 2019)

320 3.3.3. Model of landslide sediment supply potential

321 Debris flow occurrence depends on both intrinsic catchment conditions, such as
322 available loose material and steep terrain, and external triggering by rainfall. In this
323 study, landslide information is used as a proxy for sediment supply rather than as a
324 direct measure of debris-flow activity. Therefore, a LSSP model was constructed to
325 quantify the relative potential of each catchment to supply loose material. By
326 integrating LAD, SDI, RSDI, and channel gradient, the model captures the amount,
327 spatial accessibility, and topographic mobilization potential of sediment supply. LSSP
328 is calculated as follows:

$$LSSP=\frac{LAD*RSDI_{outlet}*RSDI_{channel}*J}{SDI} \quad (10)$$

329 where $RSDI_{outlet}$ and $RSDI_{channel}$ represent the relative spatial distribution index of active

landslides relative to the outlet and main channel of the catchment, respectively. LSSP represents the relative landslide sediment supply potential of a catchment. Because LAD, SDI, and RSDI are dimensionless indices and J is expressed as channel gradient (‰), LSSP should be interpreted as a relative index rather than a direct measurement of sediment volume.

3.4. Debris-flow activity intensity model

3.4.1. Precipitation index

Rainfall triggering of debris flows is commonly described using intensity–duration (I–D) relationships, which account for both rainfall intensity and event duration (Chang et al., 2021; Guzzetti et al., 2008). However, rainfall thresholds are not static after large earthquakes because sediment supply, grain-size characteristics, and vegetation cover evolve with time (Domènech et al., 2019). Abundant coseismic loose material can lower rainfall thresholds and increase sensitivity to short-duration high-intensity rainfall.

Rather than deriving site-specific I–D thresholds, this study adopted representative rainfall indices associated with documented debris flow events reported in previous studies (Guo et al., 2017; Tan and Han, 1992; Yang et al., 2021). In Equation. (11), I represents the hourly rainfall intensity of these documented triggering events, rather than long-term mean rainfall. This simplified treatment allows rainfall forcing to be incorporated consistently into the long-term catchment-scale analysis, while avoiding event-scale prediction.

Several major rainfall events during the post-earthquake period, particularly those

in 2013 and 2019, were considered as representative triggering cases. These events were characterized by high short-duration rainfall intensities typical of debris flow initiation in mountainous regions, and have been widely reported as key drivers of post-earthquake debris-flow activity. For the long-term extrapolation, no future rainfall scenario was imposed. The fitted trend is based on the calculated AI_{DF} time series and therefore represents the temporal evolution of debris-flow activity under the historical triggering-rainfall framework, rather than a prediction of future event-specific rainfall conditions.

3.4.2. Model of the intensity of debris-flow activity

To evaluate the long-term evolution of debris-flow activity intensity in the earthquake-affected area, mean LSSP for each selected year was combined with representative hourly rainfall intensity of documented debris flow triggering events. The resulting debris-flow activity intensity index (AI_{DF}) incorporates both intrinsic sediment supply conditions and rainfall forcing. The model is formulated as follows:

$$AI_{DF}=\overline{LSSP}*I \quad (11)$$

where AI_{DF} is the debris-flow activity intensity index, $\overline{LSSP}$ is the mean landslide sediment supply potential for a given year, and I is the representative hourly rainfall intensity associated with documented debris flow triggering events (mm/h). AI_{DF} is used as a relative index for temporal comparison rather than as a direct measure of debris-flow magnitude.

3.5 Spatiotemporal analysis of debris-flow activity

Based on the AI_{DF} values derived from the multi-temporal datasets, the temporal evolution of debris-flow activity was analyzed to identify post-earthquake trends. Time-series fitting was then used to characterize the long-term decay pattern and to divide the post-earthquake evolution into three stages: active, recession, and relatively stable stages.

4. Results

4.1 Spatiotemporal distribution of landslides

Coseismic landslides were delineated from the 2008 post-earthquake remote sensing images, and post-earthquake remobilized landslides were identified from images acquired in 2011, 2012, 2013, 2015, and 2019 (Fig. 6). In 2008, 9847 coseismic landslides were mapped in the study area, with a total area of 122.05 km², accounting for approximately 27.73% of the study area. The spatial distribution of active landslides became more concentrated in the northern part of the study area during the post-earthquake period (Fig. 6b–f). This pattern may be related to faster vegetation recovery in the southern catchments, where precipitation is relatively higher than in the northern part of the study area. Active landslides also tended to occur at relatively higher elevations from 2008 to 2019, as illustrated by catchments DF06 and DF28 in Fig. 6. This may indicate that loose material in lower hillslope and channel areas was preferentially remobilized and transported out of the catchments during rainfall events in the years following the earthquake (Shi et al., 2021).

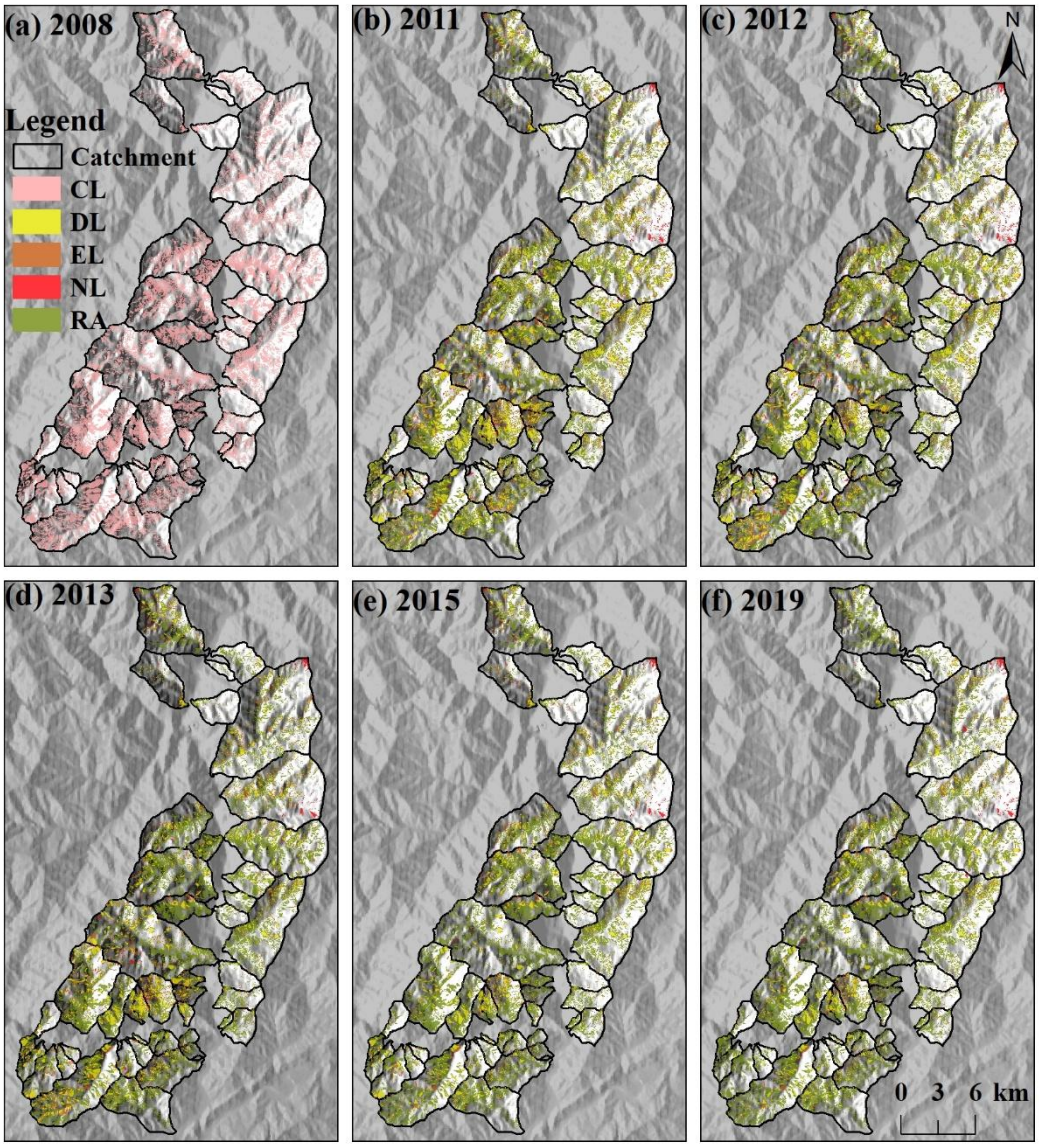


Fig. 6 Multitemporal landslide maps based on remote sensing scenes acquired in 2008 (after the M8.0 earthquake), 2011 (after the 8.10 debris flow), 2012 and 2013 (after the 7.13 debris flow), 2015 and 2019 (after the 8.20 debris flow). CL, coseismic landslides; DL, dormant landslides; EL, enlarged landslides; NL, new landslides; RA, recovery areas.

The temporal changes in landslide-affected area are summarized in Fig. 7. The total landslide-affected areas in 2011, 2012, 2013, 2015, and 2019 were 148.64, 141.73, 146.22, 136.01, and 134.26 km², respectively. Although the total landslide-affected area remained large, the active landslide area decreased markedly from 122.05 km² in 2008

to 30.55 km² in 2019, accounting for only 6.94% of the study area. Meanwhile, recovery areas expanded progressively, and the vegetation recovery rate on coseismic landslides reached 84.97% by 2019 (Fig. 7). These changes indicate a gradual reduction in active sediment sources after the Wenchuan earthquake, despite local remobilization during major rainfall events.

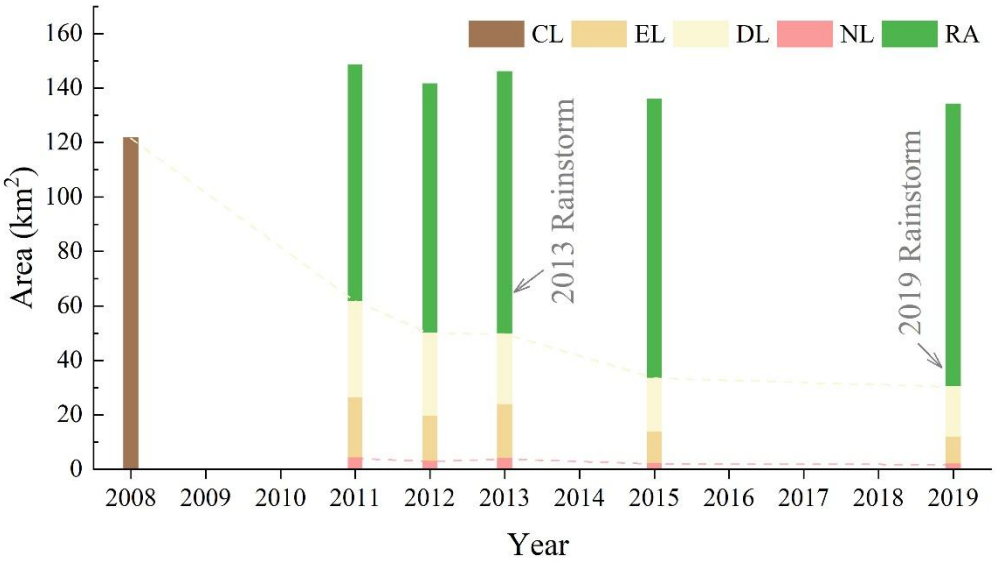


Fig. 7 Variation in landslide-affected area after the Wenchuan earthquake. CL, coseismic landslides; DL, dormant landslides; NL, new landslides; EL, enlarged landslides; RA, recovery areas. (Unit: km²).

4.2 Long-term changes in landslide debris supply

4.2.1 Change in landslide areal density

Landslide areal density (LAD) was calculated for each catchment from 2008 to 2019 using Equation. (1). As shown in Fig. 8, LAD ranged from 0 to 0.56, with the highest values occurring in 2008 immediately after the Wenchuan earthquake. In addition, the landslide areal density within the debris flow catchment tended to decrease

after the Wenchuan earthquake, even though rainstorms hit in 2013 and 2019, and the decrease was rapid during the first five years after the earthquake and then became more gradual (as observed in Fig. 8 from 2008 to 2019). This pattern indicates a progressive decline in landslide activity, probably associated with material consolidation and grain coarsening over time (Domènech et al., 2019).

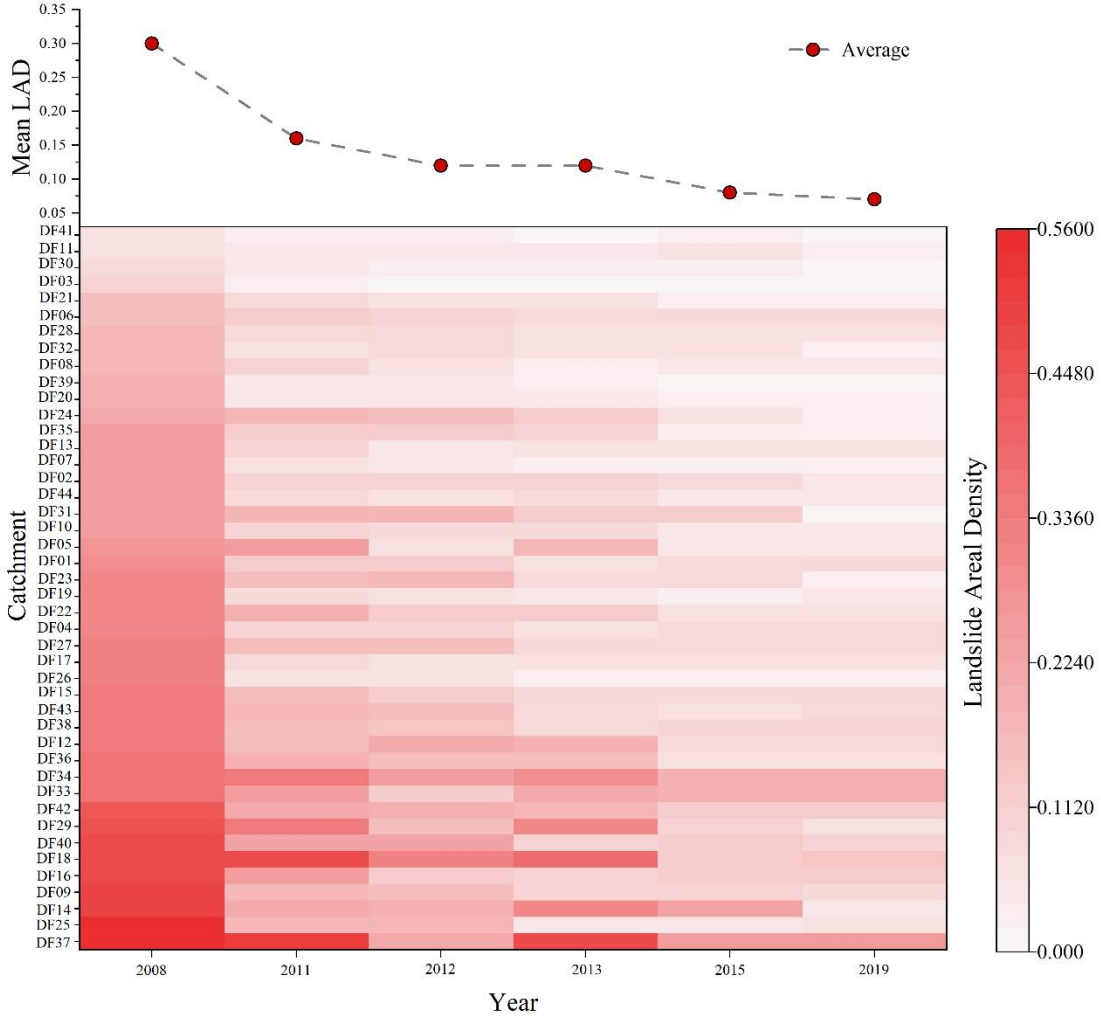


Fig. 8 Changes of landslide areal density over time

4.2.2 Spatial distribution characteristics of loose material

Fig. 9 presents the temporal changes in the spatial distribution parameters of sediment supply in the study area, with the detailed values listed in Table S2. In 2008,

most catchments had SDI values below 0.5, indicating that coseismic landslides were mainly located below the median elevation of the catchments. After 2008, the SDI values generally increased and remained close to 0.5, suggesting a gradual upward shift in the distribution of active landslides during the post-earthquake period (Fig. 9c). However, the temporal patterns varied among catchments: some showed an initial increase followed by a decrease, whereas others exhibited a continuous increase. These variations may reflect differences in local topography, sediment redistribution, and rainfall-induced remobilization of landslide material (Fan et al., 2018).

The relative spatial distribution indices indicate a gradual reduction in the connectivity between active landslides and the main sediment-transfer pathways. Specifically, the $RSDI_{outlet}$ values generally decreased from 2008 to 2019, indicating that active landslides became progressively farther from the catchment outlet. By contrast, $RSDI_{channel}$ remained higher than $RSDI_{outlet}$ throughout the observation period, suggesting that loose material remained spatially closer to the main channel than to the catchment outlet (Fig. 9b, c). These changes indicate a weakening connection between active landslides and the catchment outlet, while part of the loose material remained distributed near the main channel. Consequently, the delivery of loose material to debris flow transport pathways was gradually reduced, contributing to the decline in debris-flow activity.

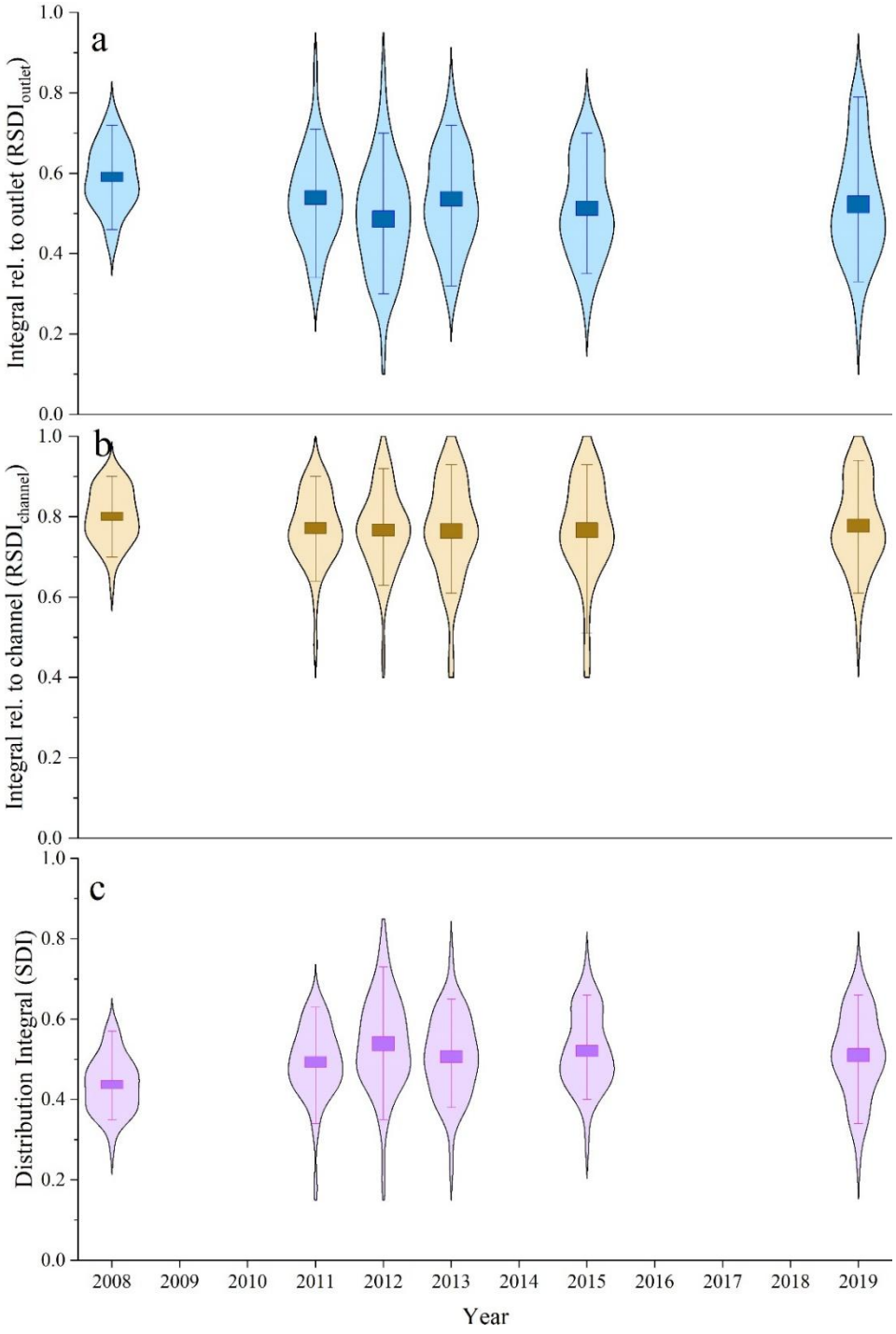


Fig. 9 Quantitative parameters of spatial distribution of sediment supply in study area. SDI denotes the spatial distribution index; $RSDI_{outlet}$ and $RSDI_{channel}$ denote the relative spatial distribution indices with respect to the catchment outlet and main channel, respectively. Detailed values are

provided in Table S2.

4.2.3 Evolution of landslide sediment supply potential

In this study, LSSP was used to quantify the intrinsic potential of each catchment to supply landslide-derived loose material to debris flow channels, rather than debris-flow activity intensity itself. Higher LSSP values indicate greater sediment availability and, under comparable triggering conditions, a higher predisposition to debris flow initiation.

The temporal evolution of LSSP is shown in Fig. 10. Before the Wenchuan earthquake, LSSP was low in most catchments, consistent with limited landslide activity and relatively high vegetation cover reported before the earthquake (Fan et al., 2019a; Yunus et al., 2020). Following the 2008 earthquake, LSSP increased sharply, and the catchment-mean value reached its highest level in 2008, as shown by the red line in Fig. 10. This increase reflects the widespread generation of coseismic landslide deposits.

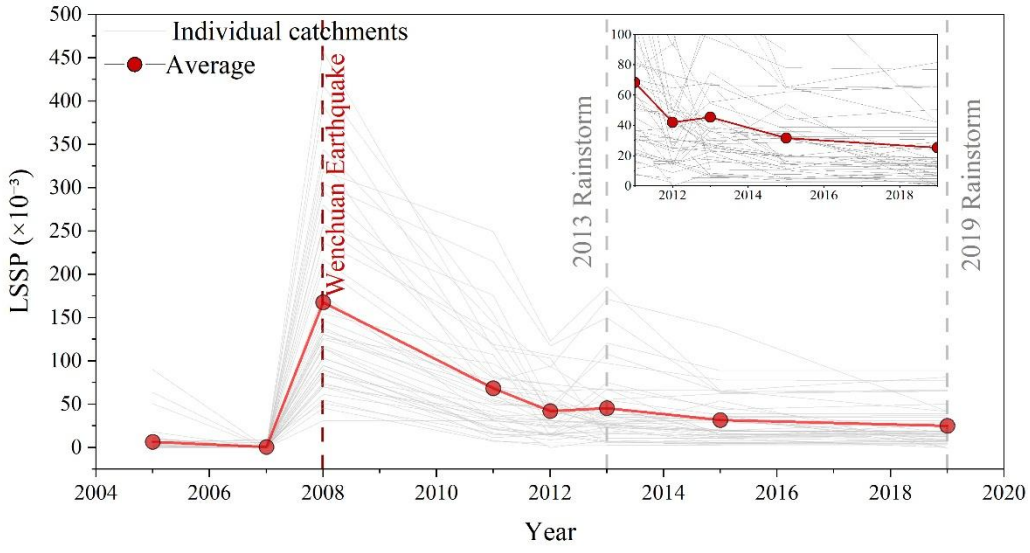


Fig. 10 Evolution of the LSSP over time ($\times 10^{-3}$)

After 2008, LSSP decreased rapidly until 2011 and then declined more slowly towards 2019. The mean trend indicates a two-stage decay pattern, with rapid early depletion of readily mobilized material followed by a slower adjustment phase associated with progressive slope stabilization and deposit consolidation. A slight rebound in LSSP is observed around 2013, coinciding with a documented rainstorm event. This response likely reflects the remobilization of previously deposited material under intense rainfall forcing. In contrast, no comparable increase is evident around the 2019 rainfall event, suggesting that the available loose material had become more limited by that time.

Individual catchments, shown by the grey lines in Fig. 10, display considerable variability, reflecting spatial heterogeneity in post-earthquake sediment supply. Nevertheless, most catchments show an overall decline in LSSP after 2008. Based on the classification thresholds in Table 3, the catchment-mean LSSP shows a low–high–medium sequence: a low level before the earthquake, a high level immediately after the earthquake, and medium during the later post-earthquake period. This pattern indicates that sediment supply remained higher than the pre-earthquake condition for several years, but progressively weakened with time.

Table 3 Classification for the LSSP in strong earthquake zones ($\times 10^{-3}$)

LSSP	LSSP＜1	1≤LSSP≤45	LSSP＞45
Classification	Low	Medium	High

Debris-flow activity should therefore be interpreted as the combined effect of

483 sediment supply and external triggering, primarily rainfall. Although the supply
484 capacity of loose material declined after 2008, residual sediment remained available in
485 many catchments. Under heavy rainfall conditions, this remaining material may still
486 contribute to debris flow occurrence, consistent with observations of prolonged post-
487 earthquake geohazard activity in the Wenchuan earthquake-affected region (Francis et
488 al., 2022; Huang and Li, 2014; Yunus et al., 2020; Zhang et al., 2023).

489 4.3 Long-term evolution of debris-flow activity intensity

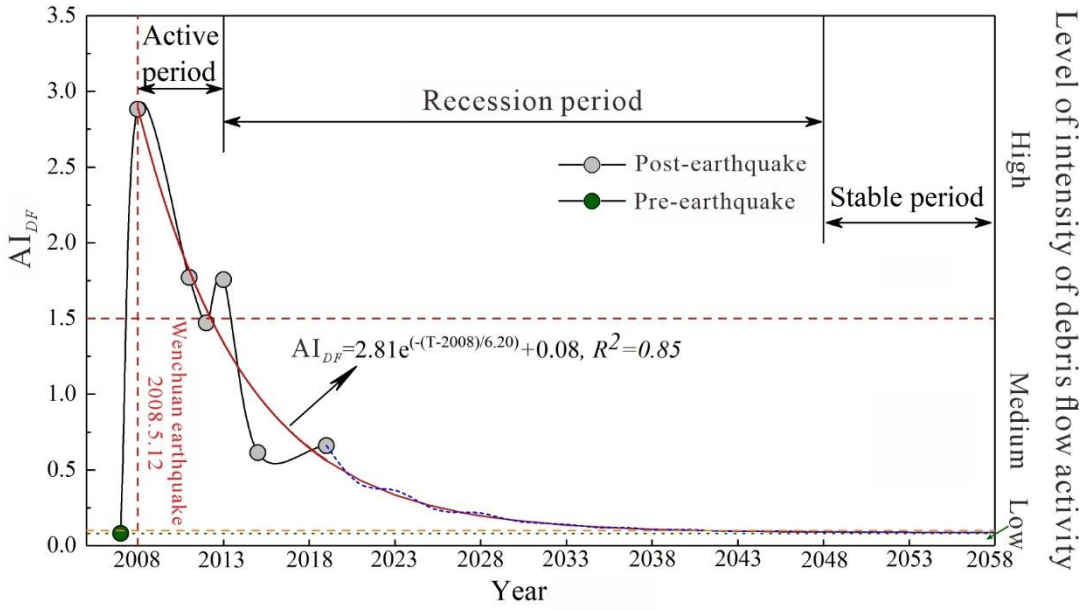
490 AI_{DF} was calculated by combining the mean LSSP with representative hourly
491 rainfall intensities of documented debris-flow triggering events (Equation. 11; Table 4).
492 Although LSSP generally decreased after 2008, AI_{DF} fluctuated because of variations
493 in rainfall forcing. AI_{DF} remained higher than the pre-earthquake level throughout the
494 observation period. For example, the mean intensity of debris flow ($\overline{AI_{DF}}$) was 0.66 in
495 2019, compared with 0.08 before the earthquake (Table 4).

496 Based on previous studies and the calculated AI_{DF} values, AI_{DF} was classified as
497 low ($AI_{DF} < 0.1$), medium ($0.1 \leq AI_{DF} \leq 1.5$), or high ($AI_{DF} > 1.5$). During 2008–2013,
498 debris-flow activity intensity remained at medium to high levels. AI_{DF} decreased from
499 2008 to 2012, but increased from 1.47 in 2012 to 1.76 in 2013, coinciding with a major
500 rainfall-triggered debris-flow event with an hourly rainfall intensity of 39.56 mm/h
501 (Table 4).

502 **Table 4** The intensity of debris-flow activity pre- and post-earthquake, the data of
503 rainfall obtained from previous studies.

Year	$\overline{LSSP}$	I (mm/h)	AI_{DF} (relative index)	Source of rainfall data
Pre-earthquake	0.001	60	0.08	(Tan and Han, 1992)
2008	0.158	18.2	2.88	
2011	0.064	27.88	1.77	
2012	0.040	36.41	1.47	(Guo et al., 2017)
2013	0.044	39.56	1.76	
2015	0.030	20.53	0.62	
2019	0.027	24.2	0.66	(Yang et al., 2021)

To quantify the post-earthquake evolution of debris-flow activity, AI_{DF} was fitted against time (Fig. 11). Before the Wenchuan earthquake, AI_{DF} was low (0.08), which was taken as the reference level. After 2008, AI_{DF} increased sharply and then declined over time. The fitted trend suggests three stages of post-earthquake debris-flow activity: an active period from 2008 to 2013, a recession period from 2013 to 2048, and a relatively stable period after 2048. The latter two stages are inferred from the fitted trend and should be interpreted as a long-term tendency rather than a direct observation or a prediction of future rainfall conditions.



512

513 **Fig. 11** Long-term evolution trend of debris-flow activity intensity in the study area. The green

514 and grey dots represent pre- and post-earthquake AI_{DF} values calculated from mean LSSP and

515 representative hourly rainfall intensities of documented triggering events. The red curve shows the

516 fitted temporal trend of AI_{DF} after the Wenchuan earthquake. The extrapolated part of the fitted

517 curve represents the long-term tendency of the calculated index and does not prescribe future

518 rainfall conditions. The horizontal dotted lines indicate the thresholds separating high, medium,

519 and low activity levels; the green dotted line indicates the pre-earthquake reference level.

520 4.4 Model validation using observed debris flow events

521 To evaluate the reliability of the proposed model, documented debris-flow events

522 after the Wenchuan earthquake were compiled from published datasets and field

523 investigations. According to Wang et al. (2022), 186 debris-flow events affecting 79

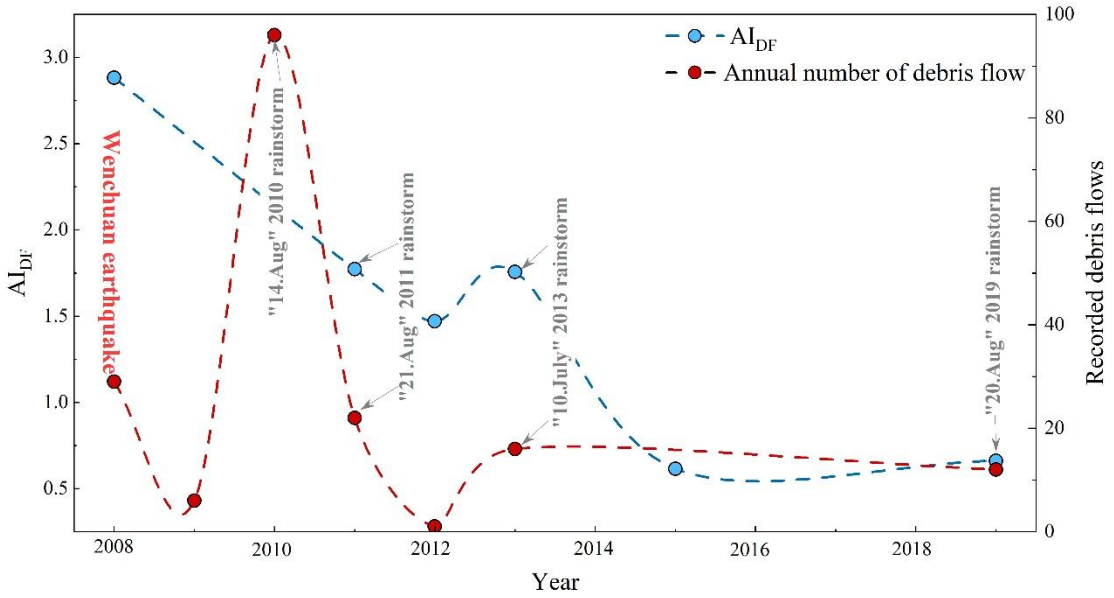
524 catchments were recorded between 2008 and 2020, with information on occurrence

525 time, deposition volume, and spatial extent. Several major rainfall-triggered events,

526 particularly those in 2010, 2013, and 2019, were selected for comparison because they
527 have been widely reported and were characterized by large sediment volumes, long
528 runout distances, and substantial downstream impacts (Huang et al., 2016; Tang et al.,
529 2012b; Xiong et al., 2021; Yang et al., 2021).

530 Fig. 12 compares the AI_{DF} with the annual number of recorded debris-flow events.
531 A positive correspondence is observed between the two series. Peaks in the observed
532 debris-flow record generally coincide with high AI_{DF} values, particularly during the
533 major rainfall-triggered activity around 2010 and 2013. After 2013, both AI_{DF} and
534 debris-flow frequency show an overall decreasing trend, indicating a gradual reduction
535 in debris-flow activity as loose material availability declined.

536 Although discrepancies occur in some years, such as 2011–2012, the overall
537 temporal patterns remain consistent. The model does not explicitly simulate event-scale
538 parameters such as deposition volume or runout distance, but it captures the main
539 temporal evolution of debris-flow activity at the catchment scale. This agreement
540 supports the use of AI_{DF} as a proxy for assessing long-term post-earthquake debris-flow
541 activity (Iverson, 1997).



542

543 **Fig. 12** Temporal comparison between AI_{DF} and observed debris flow frequency from 2008 to 2019

544 in the Wenchuan earthquake-affected area. The blue dashed line with circles represents AI_{DF}, and

545 the red dashed line with circles represents the annual number of recorded debris-flow events. Major

546 rainfall-triggered debris-flow events are annotated.

547 # 5. Discussion

548 ## 5.1 Advantages and applicability of the AI_{DF} model

549 Debris-flow activity in earthquake-affected catchments is controlled by the

550 combined effects of sediment supply, topography, and rainfall (Takahashi, 1981; Tang

551 et al., 2011). Previous studies have provided important insights into these controls. For

552 example, rainfall intensity–duration models have been developed using regional debris-

553 flow records from the Wenchuan earthquake area (Yang et al., 2021), and long-term

554 changes in landslide sediment connectivity and channel sediment supply have been

555 examined using multi-temporal inventories (Xiong et al., 2021). However, these studies

556 generally emphasize individual controls or limited combinations of controls.

557 The AI_{DF} model proposed in this study integrates LSSP, channel gradient, and
558 representative hourly rainfall intensity into a single catchment-scale index. This
559 integration allows the temporal evolution of debris-flow activity to be evaluated in a
560 consistent framework. The model is not intended to predict the magnitude of individual
561 debris-flow events, but to provide a relative measure of long-term activity intensity
562 among different post-earthquake stages. This makes it useful for comparing catchments
563 and for identifying periods when debris-flow activity remains elevated after a strong
564 earthquake.

565 5.2 Long-term evolution of debris-flow activity

566 Compared with the extensive research on coseismic landslides and vegetation
567 recovery, the long-term evolution of post-earthquake debris-flow activity remains less
568 well constrained. Previous studies suggested that enhanced landslide activity after the
569 Wenchuan earthquake may last for about 10–20 years, based on landslide inventories
570 and vegetation recovery (Fan et al., 2018; Tang et al., 2016; Yang et al., 2018b; Yunus
571 et al., 2020). Other studies indicated that post-earthquake debris-flow activity may
572 persist for more than 20 years because of the long-term storage and remobilization of
573 coseismic sediment (Huang and Li, 2014; Zhang and Zhang, 2017; Xiong et al., 2021).

574 The results of this study support the view that debris-flow activity can remain
575 elevated for several decades after a large earthquake. The fitted AI_{DF} trend shows a
576 rapid post-earthquake increase followed by a gradual decline, reflecting the progressive
577 depletion, redistribution, and stabilization of landslide-derived sediment. This long-

term decline is consistent with reductions in active landslide area, decreasing LSSP, and weakening connectivity between sediment sources and debris-flow transport pathways. Nevertheless, the decline is not monotonic. Major rainfall events can temporarily increase debris-flow activity by remobilizing residual loose material, as indicated by the increase in AI_{DF} around 2013.

The comparison between modeled AI_{DF} and recorded debris-flow frequency further suggests that the proposed index captures the main temporal pattern of post-earthquake debris-flow activity. The agreement is strongest during major rainfall-triggered periods, such as 2010 and 2013, when both abundant sediment availability and intense rainfall contributed to high debris-flow activity (Fig. 12). Some discrepancies between modeled and observed activity are expected because rainfall is spatially variable and event records are incomplete. Therefore, AI_{DF} should be interpreted as a catchment-scale indicator of long-term activity tendency rather than an event-scale prediction tool.

5.3 Limitations

Although the proposed framework provides a quantitative assessment of long-term debris-flow activity, several limitations remain. First, rainfall forcing was represented by representative hourly rainfall intensity, whereas cumulative rainfall, antecedent rainfall, and rainfall duration can also influence debris-flow initiation. These factors should be incorporated when more complete rainfall records become available. Second, most rainfall data were obtained from stations near catchment outlets, which may not

fully represent rainfall conditions in the actual initiation zones. Orographic variations in rainfall may therefore introduce uncertainty into the estimated AI_{DF} values. Third, the model focuses mainly on landslide-derived sediment supply from hillslopes and does not explicitly quantify sediment already stored within channels. As hillslope deposits are progressively transferred into channels after the earthquake, channel sediment storage and remobilization may become increasingly important. Finally, model validation was based on documented debris-flow events rather than direct simulation of event magnitude, such as volume, peak discharge, or runout distance. Despite these limitations, the framework provides a practical basis for evaluating long-term changes in debris-flow activity where continuous field measurements are limited.

6. Conclusions

The 2008 Wenchuan earthquake generated widespread coseismic landslides and supplied large amounts of loose material on hillslopes and channels in the epicentral area. In this study, a catchment-scale framework was developed to evaluate the long-term evolution of debris-flow activity by integrating LSSP, topographic conditions, and representative hourly rainfall intensity. The main conclusions are as follows:

(1) Multi-temporal landslide inventories show a clear reduction in active sediment sources after the earthquake. The active landslide area decreased from 122.05 km^2 in 2008 to 30.55 km^2 in 2019, while recovery areas expanded progressively. During the post-earthquake period, active landslides became more concentrated in the northern part of the study area and tended to occur at relatively higher elevations. These changes

620 indicate a gradual weakening of the connection between landslide-derived sediment and
621 debris-flow transport pathways.
622 (2) LSSP increased sharply immediately after the earthquake because of the
623 widespread generation of coseismic landslide deposits, and then declined over time.
624 The decline was rapid during 2008–2011 and became more gradual afterwards,
625 reflecting the depletion of readily mobilized material, progressive slope stabilization,
626 and deposit consolidation. Nevertheless, LSSP in many catchments remained higher
627 than the pre-earthquake level in 2019, indicating that residual loose material was still
628 available for debris-flow initiation under suitable rainfall conditions.
629 (3) The AI_{DF} calculated by combining mean LSSP with representative hourly
630 rainfall intensity, captured the main temporal pattern of observed debris-flow activity.
631 AI_{DF} decreased overall after its post-earthquake peak, although short-term increases
632 occurred during major rainfall events. The fitted long-term trend suggests three stages
633 of post-earthquake debris-flow activity: an active period from 2008 to 2013, a recession
634 period from 2013 to 2048, and a relatively stable period after 2048. The latter two stages
635 are inferred from the fitted trend and should be interpreted as a long-term tendency
636 rather than a prediction of future rainfall conditions.
637 Overall, the results indicate that debris-flow activity in the Wenchuan earthquake-
638 affected area may persist for several decades, mainly controlled by the gradual
639 depletion, redistribution, and stabilization of landslide-derived sediment under rainfall
640 forcing. The proposed framework provides a quantitative basis for assessing long-term

641 debris-flow activity in earthquake-affected mountain catchments.

642 Declaration of Competing Interest

643 The authors declare that they have no known competing financial interests or
644 personal relationships that could have appeared to influence the work reported in this
645 paper.

646 Reference

647 Chang, M., Dou, X., Hales, T. C., and Yu, B., 2021, Patterns of rainfall-threshold for deb
648 ris-flow occurrence in the Wenchuan seismic region, Southwest China: Bulletin of Eng
649 ineering Geology and the Environment, v. 80. https://doi.org/10.1007/s10064-020-02080
650 -7.

651 Chen, M., Tang, C., Li, M., Xiong, J., Luo, Y., Shi, Q., Zhang, X., Tie, Y., and Feng, Q.,
652 2022, Changes of surface recovery at coseismic landslides and their driving factors i
653 n the Wenchuan earthquake-affected area: Catena, v. 210, 105871. https://doi.org/10.10
654 16/j.catena.2021.105871.

655 Chen, M., Tang, C., Xiong, J., Shi, Q. Y., Li, N., Gong, L. F., Wang, X. D., and Tie, Y.,
656 2020, The long-term evolution of landslide activity near the epicentral area of the 2
657 008 Wenchuan earthquake in China: Geomorphology, v. 367, 107317. https://doi.org/10.
658 1016/j.geomorph.2020.107317.

659 Cui, P., Guo, X., Yan, Y., Li, Y., and Ge, Y., 2018, Real-time observation of an active debris flow
660 watershed in the Wenchuan Earthquake area: Geomorphology, v. 321, p. 153-166.
661 https://doi.org/10.1016/j.geomorph.2018.08.024.

662 Cui, P., Zhuang, J., Chen, X., ZHang, J., and Zhou, X., 2010, Characteristics and counter
663 measures of debris flow in Wenchuan area after the earthquake: Journal of Sichuan U
664 niversity (Engineering Science Edition), Volume 42, p. 10-19. https://doi.org/10.15961/j.
665 jsuese.2010.05.004.
666 Domènech, G., Fan, X., Scaringi, G., van Asch, T. W., Xu, Q., Huang, R., and Hales, T. C., 2019,
667 Modelling the role of material depletion, grain coarsening and revegetation in debris flow
668 occurrences after the 2008 Wenchuan earthquake: Engineering geology, v. 250, p. 34-44.
669 https://doi.org/10.1016/j.enggeo.2019.01.010.
670 Fan, J., Zhang, H., Guo, F., and Liu, F., 2012, Prediction for debris flow runout zones based on
671 spatial distribution of unconsolidated material in watersheds: Science of Soil and Water
672 Conservation, v. 10, no. 2, p. 8-14. https://doi.org/10.3969/j.issn.1672-3007.2012.02.002.
673 Fan, X. M., Domènech, G., Scaringi, G., Huang, R. Q., Xu, Q., Hales, T. C., Dai, L. X., Yang, Q.,
674 and Francis, O., 2018, Spatio-temporal evolution of mass wasting after the 2008 Mw 7.9
675 Wenchuan earthquake revealed by a detailed multi-temporal inventory: Landslides, v. 15, no.
676 12, p. 2325-2341. https://doi.org/10.1007/s10346-018-1054-5.
677 Fan, X. M., Scaringi, G., Domènech, G., Yang, F., Guo, X. J., Dai, L. X., He, C. Y., Xu,
678 Q., and Huang, R. Q., 2019, Two multi-temporal datasets that track the enhanced la
679 ndsliding after the 2008 Wenchuan earthquake: Earth System Science Data, v. 11, no.
680 1, p. 35-55. https://doi.org/10.5194/essd-11-35-2019.
681 Fan, X. M., Scaringi, G., Korup, O., West, A. J., van Westen, C. J., Tanyas, H., Hovius,
682 N., Hales, T. C., Jibson, R. W., and Allstadt, K. E., 2019b, Earthquake-Induced Chain

s of Geologic Hazards: Patterns, Mechanisms, and Impacts: Reviews of Geophysics, v. 57, no. 2, p. 421-503. https://doi.org/10.1029/2018RG000626.

Fan, X., Xu, Q., van Westen, C. J., Huang, R., and Tang, R., 2017, Characteristics and classification of landslide dams associated with the 2008 Wenchuan earthquake: Geoenvironmental Disasters, 4, 12. https://doi.org/10.1186/s40677-017-0079-8.

Francis, O., Fan, X., Hales, T., Hobley, D., Xu, Q., and Huang, R., 2022, The Fate of Sediment After a Large Earthquake: Journal of Geophysical Research: Earth Surface, 127, e2021JF006352. https://doi.org/10.1029/2021JF006352.

Guo, X., Cui, P., Marchi, L., and Ge, Y., 2017, Characteristics of rainfall responsible for debris flows in Wenchuan Earthquake area: Environmental Earth Sciences, v. 76, no. 17: 596. https://doi.org/10.1155/2014/519865.

Guzzetti, F., Peruccacci, S., Rossi, M., and Stark, C., 2008, The rainfall intensity-duration control of shallow landslides and debris flows: An update: Landslides, v. 5, p. 3-17.

Hu, T., and Huang, R. Q., 2017, A catastrophic debris flow in the Wenchuan Earthquake area, July 2013: characteristics, formation, and risk reduction: Journal of Mountain Science, v. 14, no. 1, p. 15-30. https://doi.org/10.1007/s11629-016-3965-8.

Huang, R. Q., 2011, After effect of geohazards induced by the Wenchuan earthquake: Jour nal of Engineering Geology, v. 19, no. 02, p. 145-151. https://doi.org/10.3969/j.issn.10 04-9665.2011.02.001.

Huang, R. Q., Yu, B., Hu, W., Li, W. L., Fan, X. M., Tang, C., and Xu, Q., 2016, The l ong-term geologic hazards and consequent risk after the Wenchuan earthquake, Landsli

704 des and Engineered Slopes. Experience, Theory and Practice: Rome, Italy, p. 233-258.
705 https://doi.org/10.1201/b21520-21.
706 Huang, R., and Li, W., 2014, Post-earthquake landsliding and long-term impacts in the We
707 nchuan earthquake area, China: Engineering geology, v. 182, p. 111-120. https://doi.org
708 /10.1016/j.enggeo.2014.07.008.
709 Iverson, R. M., 1997, The physics of debris flows: Reviews of Geophysics, v. 35, no. 3,
710 p. 245-296. https://doi.org/10.1029/97RG00426.
711 Kargel, J., and Hudnut, K., 2016, Geomorphic and geologic controls of geohazards induce
712 d by Nepal's 2015 Gorkha earthquake: Science, v. 351. https://doi/10.1126/science.aac8
713 353.
714 Keefer, D. K., 1984, Landslides caused by earthquakes: Geological Society of America Bu
715 lletin, v. 95, no. 4. https://doi.org/10.1130/0016-7606(1984)95<406:LCBE>2.0.CO;2.
716 Li, C. R., Wang, M., and Liu, K., 2018, A decadal evolution of landslides and debris flo
717 ws after the Wenchuan earthquake: Geomorphology, v. 323, p. 1-12. https://doi.org/10.
718 1016/j.geomorph.2018.09.010.
719 Lin, C.-W., Liu, S.-H., Lee, S.-Y., and Liu, C.-C., 2006, Impacts of the Chi-Chi earthquak
720 e on subsequent rainfall-induced landslides in central Taiwan: Engineering Geology, v.
721 86, no. 2-3, p. 87-101. https://doi.org/10.1016/j.enggeo.2006.02.010.
722 Mondini, A. C., Guzzetti, F., Reichenbach, P., Rossi, M., Cardinali, M., and Ardizzone, F.,
723 2011, Semi-automatic recognition and mapping of rainfall induced shallow landslides
724 using optical satellite images: Remote Sensing of Environment, v. 115, no. 7, p. 1743

-1757. https://doi.org/10.1016/j.rse.2011.03.006.

Parker, R. N., Densmore, A. L., Rosser, N. J., de Michele, M., Li, Y., Huang, R., Whadc oat, S., and Petley, D. N., 2011, Mass wasting triggered by the 2008 Wenchuan earth quake is greater than orogenic growth: Nature Geoscience, v. 4, no. 7, p. 449-452. ht tps://doi.org/10.1038/ngeo1154.

Shen, P., Zhang, L. M., Fan, R. L., Zhu, H., and Zhang, S., 2020, Declining geohazard activity with vegetation recovery during first ten years after the 2008 Wenchuan earthquake: Geomorphology, v. 352, 106989. https://doi.org/10.1016/j.geomorph.2019.106989.

Shi, Q. Y., Tang, C., Gong, L. F., Chen, M., Li, N., Zhou, W., Xiong, J., Tang, H., Wang, X. D., and Li, M. W., 2021, Activity evolution of landslides and debris flows after the Wenchuan earthquake in the Qipan catchment, Southwest China: Journal of Mountain Science, v. 18, no. 4, p. 932-951. https://doi.org/10.1007/s11629-020-6494-4.

Strahler, A., 1952, Hypsometric (Area Altitude) Analysis of Erosional Topology: Geological Society of America Bulletin, v. 63, p.1117-1142. https://doi.org/10.1130/0016-7606(195 2)63[1117:HAAOET]2.0.CO;2.

Takahashi, T., 1981, Estimation of potential debris flows and their hazardous zones: J Nat Disaster Sci, v. 3, p. 57-89.

Tan, W., and Han, Q., 1992, Study on regional critical rainfall indices of debris flow in S ichuan Province: Journal of catastrophology, v. 7, no. 02, p. 37-42. https://doi.org/CN KI:SUN:ZHXU.0.1992-02-007.

Tang, C., van Asch, T. W. J., Chang, M., Chen, G. Q., Zhao, X. H., and Huang, X. C., 2012a,

Catastrophic debris flows on 13 August 2010 in the Qingping area, southwestern China: The combined effects of a strong earthquake and subsequent rainstorms: Geomorphology, v. 139-140, p. 559-576. https://doi.org/10.1016/j.geomorph.2011.12.021.

Tang, C., Westen, C. J. V., Tanyas, H., and Jetten, V. G., 2016, Analysing post-earthquake landslide activity using multi-temporal landslide inventories near the epicentral area of the 2008 Wenchuan earthquake: Natural Hazards & Earth System Sciences, v. 16, 2641–2655. https://doi.org/10.5194/nhess-16-2641-2016.

Tang, C., Zhu, J., Chang, M., Ding, J., and Qi, X., 2012b, An empirical–statistical model for predicting debris flow runout zones in the Wenchuan earthquake area: Quaternary International, v. 250, p. 63-73. https://doi.org/10.1016/j.quaint.2010.11.020.

Tang, C., Zhu, J., Ding, J., Cui, X. F., Chen, L., and Zhang, J. S., 2011, Catastrophic debris flows triggered by a 14 August 2010 rainfall at the epicenter of the Wenchuan earthquake: Landslides, v. 8, no. 4, p. 485-497. https://doi.org/10.1007/s10346-011-0269-5.

Utley, I., Hales, T., Hussain, E., and Fan, X., 2025, Transformations in exposure to debris flows in post-earthquake Sichuan, China: Nat. Hazards Earth Syst. Sci., v. 25, no. 8, p. 2699-2716.

Wang, L., Chang, M., Le, J., Xiang, L., and Ni, Z., 2022, Two multi-temporal datasets to track debris flow after the 2008 Wenchuan earthquake: Scientific Data, v. 9. https://doi.org/10.1038/s41597-022-01658-y.

Wu, S., Shi, J., and Wang, H., 2012, Analysis of activity intensity for landslides triggered by the Wenchuan earthquake, Sichuan Province, China: Environmental Earth Sciences, v. 65,1021-1028. https://doi.org/10.1007/s12665-011-0952-9.

Xiong, J., Tang, C., Chen, M., Gong, L., Li, N., Zhang, X., and Shi, Q., 2021, Long-term changes

768 in the landslide sediment supply potential for debris flow occurrence in Wenchuan County,
769 China: Catena, v. 203. https://doi.org/10.1016/j.catena.2021.105340.
770 Xiong, J., Tang, C., Tang, H., Chen, M., Xianzheng, Z., Shi, Q., Chang, M., Gong, L., L
771 i, N., and Li, M., 2022, Long-term hillslope erosion and landslide–channel coupling i
772 n the area of the catastrophic Wenchuan earthquake: Engineering Geology, v. 305, p.
773 106727. https://doi.org/10.1016/j.enggeo.2022.106727.
774 Xu, C., Xu, X., Yao, X., and Dai, F., 2014, Three (nearly) complete inventories of landsli
775 des triggered by the May 12, 2008 Wenchuan Mw 7.9 earthquake of China and their
776 spatial distribution statistical analysis: Landslides, v. 11, no. 3, p. 441-461. https://doi.
777 org/10.1007/s10346-013-0404-6.
778 Xu, Q., Zhang, S., Li, W.-l., and Asch, T. W. J., 2012, The 13 August 2010 catastrophic debris flows
779 after the 2008 Wenchuan earthquake, China: Natural Hazards and Earth System Sciences, v.
780 12, p. 201-216. https://doi.org/10.5194/nhess-12-201-2012.
781 Yang, F., Fan, X., Siva Subramanian, S., Dou, X., Xiong, J., Xia, B., Yu, Z., and Xu, Q.,
782 2021, Catastrophic debris flows triggered by the 20 August 2019 rainfall, a decade s
783 ince the Wenchuan earthquake, China: Landslides, v. 18, no. 9, p. 3197-3212. https://d
784 oi.org/10.1007/s10346-021-01713-6.
785 Yang, F., Fan, X., Wei, Z., and Xu, Q., 2022, Modelling the evolution of debris flows aft
786 er the 2008 Wenchuan earthquake, Engineering Geology, https://doi.org/10.1016/j.engge
787 o.2023.107152.
788 Yang, W. T., Qi, W. W., and Zhou, J. X., 2018b, Decreased post-seismic landslides linked to

789 vegetation recovery after the 2008 Wenchuan earthquake: Ecological indicators, v. 89, p. 438-
790 444. https://doi.org/10.1016/j.ecolind.2017.12.006.
791 Yang, W., Qi, W., and Zhou, J., 2018a, Effects of precipitation and topography on vegetation
792 recovery at landslide sites after the 2008 Wenchuan earthquake: Land Degradation &
793 Development, v. 29, no. 10, p. 3355-3365. https://doi.org/10.1002/ldr.3098.
794 Yu, B., Ma, Y., and Wu, Y., 2012, Case study of a giant debris flow in the Wenjia Gully, Sichuan
795 Province, China: Natural Hazards, v. 65, 835–849. https://doi.org/10.1007/s11069-012-0395-y.
796 Yunus, A. P., Fan, X. M., Tang, X. L., Jie, D., Xu, Q., and Huang, R. Q., 2020, Decadal vegetation
797 succession from MODIS reveals the spatio-temporal evolution of post-seismic landsliding after
798 the 2008 Wenchuan earthquake: Remote Sensing of Environment, v. 236, p. 111476.
799 https://doi.org/10.1016/j.rse.2019.111476.
800 Zhang, S., and Zhang, L. M., 2017, Impact of the 2008 Wenchuan earthquake in China on
801 subsequent long-term debris flow activities in the epicentral area: Geomorphology, v. 276, p.
802 86-103. https://doi.org/10.1016/j.geomorph.2016.10.009.
803 Zhang, S., Zhang, L., Lacasse, S., and Nadim, F., 2016, Evolution of Mass Movements near
804 Epicentre of Wenchuan Earthquake, the First Eight Years: Scientific Reports, v. 6, p. 36154.
805 https://doi.org/10.1038/srep36154.
806 Zhang, W., Chen, J., Ma, J., Cao, C., Yin, H., Wang, J., and Han, B., 2023, Evolution of sediment
807 after a decade of the Wenchuan earthquake: a case study in a protected debris flow catchment
808 in Wenchuan County, China: Acta Geotechnica. https://doi.org/10.1007/s11440-022-01789-x.
809 Zhou, W., Fang, J., Tang, C., and Yang, G., 2019, Empirical relationships for the estimation of debris

flow runout distances on depositional fans in the Wenchuan earthquake zone: Journal of Hydrology, v. 577. https://doi.org/10.1016/j.jhydrol.2019.123932.

Zhu, J., Tang, C., Chang, M., Le, M. H., and Huang, X., 2015, Field observations of the disastrous 11 July 2013 debris flows in Qipan gully, Wenchuan area, Southwestern China, Engineering Geology for Society and Territory-Volume 2, Springer, p. 531-535. https://doi.org/10.1007/978-3-319-09057-3_88.

Supplementary

Table S1 Detailed topographic information for the 44 debris flow catchments.

Debris Flow code	Debris Flow name	Area (km^2)	Channel length (km)	Relief (km)	Channel gradient (‰)
DF01	Chediguan	16.46	7.49	2.32	310.24
DF02	Chutou	21.68	8.63	2.88	333.92
DF03	Dacaotou	5.61	4.05	1.60	395.16
DF04	Dashibao	0.40	1.51	1.10	728.06
DF05	Douyaping	2.80	2.91	1.74	596.56
DF06	Fotangba	34.55	8.94	2.43	271.63
DF07	Gangou	1.42	1.92	1.05	548.40
DF08	Gaodian	7.51	4.60	2.31	502.83
DF09	Gaojia	3.78	3.19	1.78	559.95
DF10	Hongchun	5.49	3.70	1.26	341.45
DF11	Huaxi	10.32	6.36	1.90	298.13

DF12	Huanglian	24.25	10.22	2.78	272.06
DF13	Huangni	2.25	2.18	1.57	720.16
DF14	Louwailou	1.78	2.53	1.74	686.16
DF15	Luoquanwan	28.50	9.11	2.42	265.91
DF16	Luoshi	1.31	2.04	1.49	732.63
DF17	Maxi	15.78	7.60	1.86	244.94
DF18	Mayangdian	2.11	2.73	1.82	666.21
DF19	Mozi	5.52	1.17	0.86	734.40
DF20	Mujiangping	2.51	4.64	1.64	353.59
DF21	Niudaoping	3.39	3.14	1.50	479.16
DF22	Niujuan	10.68	3.27	1.84	560.97
DF23	Qingshui	3.38	6.33	1.83	289.99
DF24	Shangyanshui	2.51	3.93	2.24	570.23
DF25	Shaofang	0.62	2.96	1.85	625.43
DF26	Supodian	2.95	1.68	0.94	560.90
DF27	Taiping	27.19	2.91	1.56	537.69
DF28	Taoguan	51.71	9.11	2.28	249.70
DF29	Wasi	1.58	14.18	2.97	209.52
DF30	Wayao	1.71	2.07	1.43	692.54
DF31	Wuji	7.40	2.84	1.78	627.73
DF32	Xiayanshui	1.31	5.20	2.60	500.66

DF33	Xiangjia	1.70	2.03	1.52	747.75
DF34	Xiaojia	7.98	3.37	2.08	618.51
DF35	Xiaogou	39.94	4.38	2.39	545.02
DF36	Xiaoyin	23.54	11.15	3.16	283.56
DF37	Xiezi	3.92	3.18	2.25	707.62
DF38	Yangxianger	24.33	3.78	2.03	537.23
DF39	Yeniu	3.60	3.63	1.68	461.35
DF40	Yiwanshui	7.19	9.94	2.96	297.89
DF41	Yiwanshuixi	7.22	3.34	2.53	759.33
DF42	Yinjiaba	7.71	5.04	2.53	502.62
DF43	Yinchang	7.05	4.21	1.99	471.87
DF44	Yinxingping	1.61	5.53	2.48	447.74

818

Table S2 Quantitative parameters of the spatial distribution of sediment supply in the study area. SDI denotes the distribution integral of sediment supply; RSDI_o and RSDI_c are used as abbreviations for RSDIoutlet and RSDIchannel, representing the distribution integrals relative to the catchment outlet and the main channel, respectively.

Gully code	Year																	
	2008			2011			2012			2013			2015			2019		
	SDI	$RSDI_o$	$RSDI_c$	SDI	$RSDI_o$	$RSDI_c$	SDI	$RSDI_o$	$RSDI_c$	SDI	$RSDI_o$	$RSDI_c$	SDI	$RSDI_o$	$RSDI_c$	SDI	$RSDI_o$	$RSDI_c$
DF01	0.37	0.68	0.82	0.41	0.63	0.83	0.41	0.62	0.8	0.4	0.64	0.84	0.44	0.61	0.82	0.45	0.6	0.82
DF02	0.39	0.55	0.76	0.44	0.47	0.79	0.46	0.45	0.76	0.44	0.47	0.76	0.46	0.47	0.75	0.46	0.46	0.73
DF03	0.33	0.73	0.63	0.44	0.63	0.48	0.49	0.56	0.45	0.46	0.64	0.45	0.46	0.65	0.44	0.64	0.33	0.94
DF04	0.36	0.7	0.9	0.41	0.65	0.76	0.58	0.47	0.86	0.47	0.57	0.61	0.56	0.49	0.76	0.56	0.49	0.76
DF05	0.48	0.53	0.87	0.56	0.45	0.86	0.67	0.32	0.8	0.58	0.42	0.87	0.64	0.36	0.82	0.58	0.42	0.82
DF06	0.35	0.64	0.77	0.43	0.53	0.73	0.46	0.5	0.7	0.4	0.57	0.73	0.43	0.55	0.71	0.47	0.51	0.69

DF07	0.42	0.62	0.87	0.5	0.53	0.9	0.81	0.15	0.96	0.65	0.37	0.91	0.66	0.36	0.9	0.64	0.39	0.9
DF08	0.45	0.51	0.83	0.61	0.33	0.78	0.62	0.33	0.78	0.62	0.32	0.76	0.67	0.26	0.74	0.67	0.22	0.74
DF09	0.45	0.62	0.74	0.53	0.58	0.74	0.52	0.58	0.78	0.5	0.72	0.75	0.47	0.65	0.77	0.5	0.64	0.73
DF10	0.42	0.59	0.76	0.54	0.47	0.67	0.55	0.45	0.67	0.56	0.47	0.76	0.55	0.48	0.74	0.54	0.46	0.64
DF11	0.4	0.65	0.91	0.34	0.75	0.93	0.35	0.74	0.92	0.34	0.74	0.93	0.37	0.71	0.92	0.34	0.76	0.93
DF12	0.51	0.52	0.75	0.5	0.54	0.77	0.55	0.47	0.75	0.5	0.53	0.78	0.4	0.66	0.8	0.4	0.66	0.8
DF13	0.37	0.7	0.87	0.41	0.68	0.9	0.4	0.35	0.95	0.39	0.72	0.94	0.52	0.6	0.88	0.52	0.59	0.88
DF14	0.46	0.65	0.71	0.48	0.63	0.73	0.55	0.57	0.65	0.5	0.61	0.66	0.51	0.66	0.65	0.35	0.79	0.67
DF15	0.4	0.6	0.76	0.46	0.53	0.75	0.51	0.49	0.75	0.41	0.61	0.72	0.47	0.51	0.74	0.48	0.51	0.73
DF16	0.45	0.66	0.81	0.53	0.58	0.77	0.7	0.37	0.7	0.57	0.62	0.63	0.6	0.55	0.71	0.6	0.54	0.76
DF17	0.54	0.43	0.73	0.63	0.34	0.68	0.64	0.33	0.67	0.63	0.32	0.7	0.66	0.3	0.72	0.66	0.3	0.71
DF18	0.47	0.55	0.87	0.54	0.49	0.86	0.61	0.41	0.83	0.56	0.46	0.87	0.52	0.5	0.85	0.5	0.52	0.84

DF19	0.36	0.69	0.79	0.45	0.61	0.69	0.48	0.55	0.74	0.49	0.59	0.72	0.47	0.59	0.7	0.45	0.61	0.73
DF20	0.49	0.56	0.87	0.49	0.59	0.88	0.48	0.56	0.7	0.39	0.66	0.76	0.62	0.41	0.89	0.62	0.46	0.9
DF21	0.37	0.67	0.9	0.33	0.69	0.88	0.35	0.67	0.91	0.38	0.66	0.9	0.42	0.61	0.9	0.42	0.64	0.89
DF22	0.49	0.52	0.71	0.56	0.43	0.71	0.65	0.41	0.63	0.63	0.66	0.61	0.63	0.44	0.59	0.64	0.44	0.59
DF23	0.51	0.57	0.85	0.47	0.62	0.81	0.49	0.59	0.82	0.41	0.66	0.85	0.41	0.66	0.86	0.34	0.76	0.61
DF24	0.46	0.59	0.91	0.59	0.47	0.86	0.57	0.49	0.88	0.53	0.54	0.9	0.45	0.68	0.9	0.5	0.53	0.94
DF25	0.36	0.63	0.76	0.41	0.58	0.76	0.45	0.55	0.75	0.56	0.47	0.41	0.56	0.47	0.41	0.5	0.46	0.8
DF26	0.57	0.46	0.77	0.5	0.57	0.73	0.48	0.59	0.77	0.65	0.43	0.63	0.63	0.45	0.64	0.63	0.4	0.62
DF27	0.39	0.64	0.77	0.45	0.56	0.75	0.46	0.56	0.74	0.49	0.51	0.78	0.5	0.47	0.79	0.5	0.48	0.79
DF28	0.36	0.59	0.73	0.44	0.52	0.7	0.63	0.4	0.68	0.43	0.53	0.74	0.44	0.52	0.71	0.47	0.49	0.71
DF29	0.48	0.43	0.81	0.53	0.38	0.81	0.63	0.28	0.8	0.53	0.38	0.81	0.46	0.44	0.81	0.53	0.39	0.81
DF30	0.41	0.57	0.86	0.49	0.49	0.7	0.45	0.64	0.78	0.48	0.51	0.74	0.48	0.51	0.71	0.35	0.62	0.73

DF31	0.57	0.56	0.84	0.61	0.52	0.84	0.58	0.56	0.86	0.62	0.51	0.88	0.63	0.36	0.87	0.39	0.79	0.85
DF32	0.43	0.58	0.74	0.63	0.33	0.71	0.64	0.3	0.82	0.39	0.53	0.96	0.45	0.48	0.97	0.36	0.56	0.96
DF33	0.54	0.52	0.89	0.59	0.47	0.9	0.73	0.33	0.91	0.59	0.47	0.92	0.64	0.43	0.93	0.64	0.43	0.93
DF34	0.37	0.6	0.82	0.43	0.54	0.79	0.49	0.47	0.79	0.46	0.51	0.78	0.55	0.4	0.74	0.55	0.41	0.75
DF35	0.49	0.53	0.7	0.58	0.47	0.64	0.6	0.45	0.63	0.61	0.43	0.63	0.52	0.53	0.69	0.53	0.53	0.68
DF36	0.44	0.65	0.76	0.51	0.58	0.7	0.55	0.54	0.7	0.56	0.52	0.7	0.53	0.57	0.69	0.53	0.57	0.68
DF37	0.58	0.47	0.8	0.64	0.41	0.76	0.75	0.31	0.76	0.75	0.31	0.77	0.73	0.35	0.76	0.72	0.36	0.75
DF38	0.4	0.55	0.8	0.46	0.5	0.76	0.47	0.49	0.76	0.49	0.46	0.77	0.5	0.43	0.76	0.5	0.43	0.75
DF39	0.4	0.72	0.69	0.47	0.71	0.59	0.47	0.7	0.59	0.53	0.65	0.62	0.52	0.68	0.51	0.52	0.69	0.5
DF40	0.47	0.56	0.83	0.53	0.51	0.78	0.57	0.47	0.74	0.5	0.54	0.78	0.49	0.5	0.79	0.53	0.5	0.77
DF41	0.28	0.75	0.89	0.18	0.86	0.89	0.2	0.84	0.89	0.24	0.8	0.93	0.29	0.74	0.93	0.25	0.79	0.95
DF42	0.44	0.65	0.78	0.46	0.67	0.74	0.46	0.67	0.73	0.46	0.66	0.75	0.44	0.7	0.75	0.44	0.7	0.74

DF43	0.44	0.53	0.82	0.52	0.44	0.82	0.55	0.42	0.78	0.53	0.42	0.78	0.55	0.41	0.78	0.59	0.37	0.79
DF44	0.5	0.51	0.8	0.61	0.42	0.83	0.66	0.39	0.81	0.63	0.4	0.85	0.63	0.38	0.92	0.61	0.4	0.91

823

824